chemosensors

Article

A Porous Europium Metal–Organic Framework as a Highly Sensitive Bifunctional Sensor for Isoprocarb and Levofloxacin

You Yin [1], Yuanhong Cheng [2], Ning Song [3,*] and Chenghui Zeng [2,*]

[1] Medicine & Health Science College, Guangzhou Huashang College, Guangzhou 511300, China
[2] National Engineering Research Center for Carbohydrate Synthesis, College of Chemistry and Materials, Jiangxi Normal University, Nanchang 330022, China
[3] Jiangxi Provincial Laboratory of Advanced Metal Materials and Critical Minerals Development, Ganzhou 341000, China
* Correspondence: 15147319329@163.com (N.S.); chenghuizeng@jxnu.edu.cn (C.Z.)

Abstract

The development of highly sensitive luminescence sensing materials has attracted much attention in recent years. In this study, a new two-dimensional porous europium metal–organic framework (**EuMOF**, $[Eu(DHDA)_{1.5}\cdot 3H_2O]_n$; DHDA = 2,2-dihydroxyacetic acid) is obtained, characterized by single-crystal X-ray diffraction, powder X-ray diffraction (PXRD), scanning electron microscopy (SEM), luminescence, and Fourier transform infrared spectroscopy (FT-IR). At the best excitation at 295 nm, **EuMOF** shows red luminescence (CIE: 0.6255, 0.3740) and has four obvious peaks at 582, 605, 641, and 689 nm, which are due to $^5D_0 \rightarrow {}^7F_1$, $^5D_0 \rightarrow {}^7F_2$, $^5D_0 \rightarrow {}^7F_3$, and $^5D_0 \rightarrow {}^7F_4$ transitions, respectively. Studies have shown that **EuMOF** is a stable, fast-responding, and highly sensitive luminescence sensor for isoprocarb and levofloxacin (Lvx) in aqueous solutions, apple peel and rice extract solutions, and real urine, which are closely associated with food safety and human health. The sensing behavior toward isoprocarb and Lvx may be attributed to the specific binding of the two analytes to **EuMOF**. The sensing of isoprocarb is a dynamic luminescence-quenching process, while that of Lvx is a dynamic luminescence-enhancing process. The limits of detection (LOD) for isoprocarb and Lvx are as low as 1.0 and 0.5 nM, respectively, which are much lower than the Chinese national standard (GB 28260-2011, 2.583 μM). **EuMOF** also demonstrates strong anti-interference detection of isoprocarb in apple peel and rice extract solutions, as well as Lvx in real urine, with excellent detection stability in a 0.01~9.0 nM range. The recovery rates for isoprocarb and Lvx in real samples are 99.12%~101.25%. This work provides the first bifunctional lanthanide sensor for pesticides and antibiotics.

Keywords: lanthanide MOF; luminescence; sensor; isoprocarb; levofloxacin

Received: 21 May 2026
Revised: 11 June 2026
Accepted: 15 June 2026
Published: 22 June 2026

1. Introduction

Isoprocarb, which may remain in plants, vegetables, and fruits, can inhibit the activity of the human central and peripheral nervous system and lead to the accumulation of the neurotransmitter acetylcholine in the body, leading to acute poisoning. In addition, long-term intake of food with pesticide residue levels exceeding the recommended standards can cause chronic poisoning, endocrine disruption, reproductive disorders, dementia acceleration, and increased cancer risk [1]. Therefore, the detection and quantitative analysis of isoprocarb are highly important.

The improper use of levofloxacin (Lvx) may cause adverse symptoms, such as heart disease, central nervous system reactions, respiratory system damage, gastrointestinal damage, immune dysfunction, and impaired kidney function, and may lead to serious multi-antibiotic resistance, threatening global public health [2]. Therefore, the development of reliable and sensitive methods to detect Lvx is a current health monitoring need.

The reported methods, such as high-performance liquid chromatography, enzyme-linked immunosorbent assay, electrochemical analysis [3], spectrophotometry, chemiluminescence, capillary electrophoresis, quantum dots [4,5], and iodine determination, have high detection sensitivity and have been applied to the detection of small molecules [6,7]. However, instrumental methods, such as high-performance liquid chromatography, gas chromatography, and capillary electrophoresis [8–10], have strict requirements for the pretreatment and handling of samples. The instrumental methods suffer from several drawbacks, including long detection time, poor portability, high equipment cost, and complicated operation procedures, so it is difficult to meet the requirements for the monitoring of isoprocarb or Lvx in real-time field detection.

Metal compounds have wide applications in the field of optics [11–19], electronics [20–22], magnetism, catalysis [23–34], gas adsorption and separation [35–38], bioapplications [39–46], and so on [47,48]. As one kind of metal compound, lanthanide compounds have the unique luminescence characteristics of a large Stokes shift, long luminescence lifetime, sharp emission band, etc. [49–56]. Lanthanide ions can coordinate with various ligands to form diverse lanthanide complex structures. Since the luminescence of lanthanide ions is highly sensitive to interference from surrounding molecules, lanthanide complexes possess great application potential in luminescent sensors [57–64]. Lanthanide complexes, especially Eu^{3+}-based complexes, have the unique characteristics of rapid response, high sensitivity, and real-time monitoring ability [65–67], which overcome the shortcomings of traditional methods and provide an effective technology and application prospect for molecular detection [68,69]. Based on the above shortcomings in detection efficiency, a dual luminescence sensing system for isoprocarb and Lvx is established.

In summary, a new LnMOF ($[Eu(DHDA)_{1.5}\cdot 3H_2O]_n$, its emission wavelengths, the detection medium, and the recognition/detection mechanism of both analytes have been obtained and characterized in detail by single-crystal X-ray diffraction, powder X-ray diffraction (PXRD), scanning electron microscopy (SEM), luminescence, and Fourier transform infrared spectroscopy (FT-IR). Interestingly, **EuMOF** is a stable, fast, highly sensitive bifunctional sensor for isoprocarb and Lvx. Based on the study of luminescence lifetime, UV-visible absorption, and density functional theory (DFT), the sensing mechanisms are discussed. As an efficient pesticide sensor, **EuMOF** provides a new detection platform for isoprocarb residues in crops and has great potential application value in food safety and human health. The developed luminescence sensor can also detect Lvx in human urine effectively and quickly, which has extraordinary significance for human health and the ecological environment.

2. Materials and Methods

2.1. Synthesis of EuMOF

The ligand 2,2-dihydroxyacetic acid ($C_2H_4O_4$, DHDA, 8.51 mg, 0.092 mmol, Innochem, Beijing, China) and 1.0 mL H_2O were mixed evenly by ultrasonic treatment in a 10.0 mL flask for 5.0 min, and were adjusted to pH = 5 with NaOH. A total of 10.2 mg $Eu(NO_3)_3\cdot 6H_2O$ (0.023 mmol, prepared in the supporting information) and 1.0 mL methanol (Innochem., Beijing, China) were mixed in the second flask and sonicated for 5.0 min. The above two solutions were mixed evenly with ultrasonic treatment for

6.0 min, and then reacted for 3 days in an oven at 80°C to obtain colorless massive crystals (Figure S1). High-quality single crystals were selected for single-crystal X-ray analysis.

$[Eu(DHDA)_{1.5}\cdot 3H_2O]_n$ (EuMOF, DHDA = 2,2-dihydroxyacetic acid**)**. Yield: 35.6%, based on Eu^{3+}. Anal. Calcd (%): C, 12.51, H, 2.10. Found (%): C, 13.05; H, 2.46. FT-IR (Figure S2) (KBr pellet, cm^{-1}): 3449(s), 2828(w), 2356(w), 2339(w), 2027(w), 1636(s), 1586(w), 1387(m), 1351(m), 1269(w), 1082(s), 998(m), 769(m), 565(s), and 468(w).

2.2. Precise Structure Determination of Single Crystals

First, place the crystal in a small amount of inert dimethicone on a slide. A high-quality (crack-free and impurity-free) single crystal with regular morphology and a suitable size of 0.1–0.2 mm single crystal was picked under optical microscopy. Then, stably adhere the crystal to the center of the crystal loop and adjust the crystal position to ensure it is centered and firmly fixed, without shaking or shielding. For single-crystal testing via X-ray diffraction, power on and stabilize the single-crystal diffractometer, install the mounted crystal on the goniometer head, calibrate and center the sample through the instrument's built-in microscopy, and run the automatic centering and unit cell determination program to confirm clear, discrete diffraction spots and accurate preliminary cell parameters. After setting reasonable experimental parameters, including frame exposure time, scanning range, and diffraction angle range, perform half-sphere diffraction data collection with real-time monitoring of diffraction quality, then process the collected raw data by integrating diffraction intensity, correcting background, Lorentz, polarization, and absorption effects, and determine the precise crystal space group based on diffraction systematic absences and symmetry characteristics. Finally, solve the initial crystal structure via the direct method by conducting step-by-step structural refinement on atomic coordinates, occupancy, and thermal vibration parameters, adding hydrogen atoms reasonably, and finishing the convergence refinement until the key indices (*R*1, *wR*2, and *GOF*) meet academic standards.

2.3. Preparation of Sensing Solution

The preparation of the **EuMOF** solution: A synthesized solid sample of **EuMOF** was ground into a white powder and made into a transparent and homogeneous solution using dimethylformamide (DMF) as the solvent (1.0×10^{-3} M, calculated based on the molarity of Eu^{3+}) for later use.

The preparation of sensing solution: 50 μL of the above **EuMOF** stock solution (1.0×10^{-3} M) was mixed with 4.9 mL of deionized water and 50 μL of the tested species water solution (1.0×10^{-3} M). In the blank sample, 50 μL of the tested species solution was replaced with 50 μL of deionized water. Tap water was collected from the water tap in our laboratory. Lake water was gathered from the Yao Lake near our university. The urine samples were provided by the researcher of this work, and the serum was purchased from Innochem. These real samples were filtered with 0.45 μm membrane filters prior to the sensing test to remove solid impurities from the actual solutions.

2.4. Computational Details

Quantum chemical studies were performed using density functional theory (DFT), implemented in the GAUSSIAN 16 package [70,71]. Geometry optimization and single-point energy calculations were performed at the B3LYP functional with 6-31G(d) basis sets for other elements [72–76].

3. Results and Discussion

3.1. Crystal Structure Analysis

Single-crystal X-ray diffraction analysis reveals that **EuMOF** crystallizes in the triclinic space group *P*21/c. The crystallographic data and structural refinement parameters of **EuMOF** are listed in Table S1. **EuMOF** crystalizes in the monoclinic *P*21/c space group, with a = 11.0633(7) Å, b = 9.5274(4) Å, c = 10.0760(8) Å, α = 90°, β = 114.423(8)°, γ = 90°, V = 967.02(12) Å^3, and Z = 4. Each SBU contains one Eu^{3+}, one and a half deprotonated DHDA, and three coordinated H_2O to form a neutral unit. The lanthanide ion is coordinated by 9 O to form a polyhedral structure, where six O are from the ligand of DHDA, and the other three O are from the coordinated H_2O (Figure 1a). The ligand of DHDA adopts a chelation coordination pattern (Figure S3). Two polyhedral structures are connected to form a dinuclear cluster structure (Figure 1b); the nine coordinated O around the metal center are arranged in a single truncated quadrangular prism structure (Figure S4). Three dinuclear clusters are connected in the *ac* plane to form a single-hole structure (Figure 1c), and the hole has a diameter of 8.93 Å. It further connects in the *oa* and *oc* directions through coordination bonds to form a 2D porous MOF structure (Figure 1d). The water contact angles of the **EuMOF** (Figure S5) sheet are 77.6–78.8°, and lower than 90°, which is due to the fact that water easily forms hydrogen bonds with uncoordinated O. The coordination bond lengths are in the normal range of 2.2981–2.588 Å for coordination compounds (Table S2) [77–79].

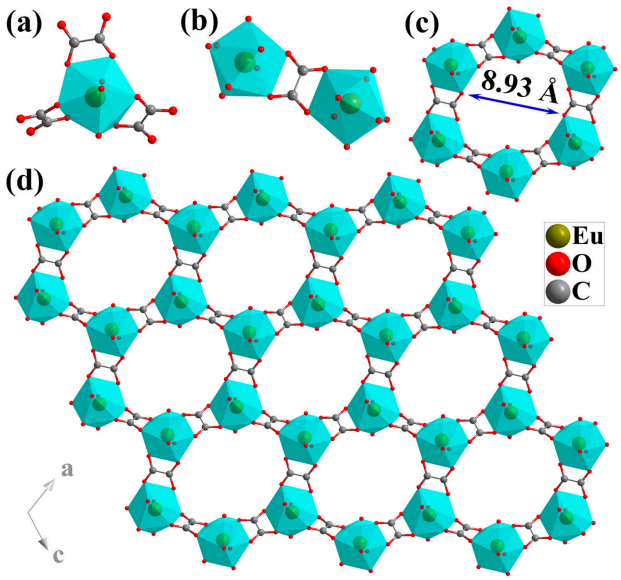

Figure 1. (**a**) The SBU structure of **EuMOF**; (**b**) the dinuclear cluster structure; (**c**) the single-hole structure constructed by three dinuclear clusters; and (**d**) the 2D porous MOF structure of **EuMOF**.

The PXRD peaks of the same batch of the as-synthesized **EuMOF** sample that soaked in pH = 2–12 water solutions, nine kinds of organic solvents of CH_3OH (MeOH), $CH_3COCH_2COCH_3$ (acetylacetone, Acac), CH_3COCH_3 (acetone), $HCON(CH_3)_2$ (N,N-dimethylformamide, DMF), CH_3CH_2OH (EtOH), CH_3CN (EtCN, acetonitrile), $(CH_3CH_2)_2O$ (ether), and water exposed in the air for 2 h or longer show that their diffraction peaks are consistent with the peaks of the original as-synthesized sample and single-crystal data (Figure 2), that is, the original material of these above samples for the stability study are from the same batch of raw material. The above results indicate the excellent stability of **EuMOF**. The scanning electron microscopy (SEM) images show that the powder sample of **EuMOF** is spherical, with particles ranging in diameter from 0.6 to 1.0 μm (Figure S6).

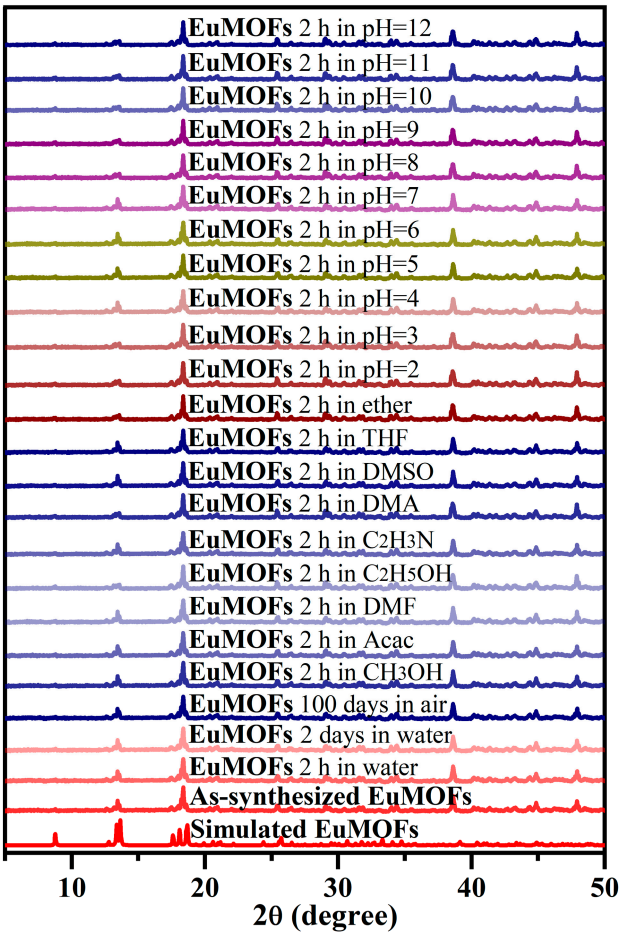

Figure 2. The PXRD pattern of **EuMOF** immersed in pH = 2–12 solutions, organic solvents, and soaked in water for 2 days and exposed in the atmosphere for 100 days.

3.2. Photophysical Studies

The photophysical properties of **EuMOF** were systematically investigated. The excitation and emission spectra, luminescence lifetimes, and the luminescence quantum yields of solid-state samples of **EuMOF** were measured at room temperature. As shown, wide excitation bands are observed in the range of 210–350 nm, which were monitored at their maximum emission peak at 605 nm (Figure 3a). At the optimal excitation of 295 nm, **EuMOF** emits four characteristic strong linear emission peaks in the range of 550–750 nm, which are due to $^5D_0 \rightarrow {}^7F_1$, $^5D_0 \rightarrow {}^7F_2$, $^5D_0 \rightarrow {}^7F_3$, and $^5D_0 \rightarrow {}^7F_4$ transitions at 582, 605, 641, and 689 nm, respectively (Figure 3a) [80], and which is a pure red luminescence (CIE: 0.6255, 0.3740; Figure 3b). The photoluminescence quantum yield of **EuMOF** is a relatively high value of 9.81%. The maximum emission (605 nm) of the $^5D_0 \rightarrow {}^7F_2$ transition was selected to monitor its luminescence lifetime, which fits a double exponential function (Figure 3c) and shows a long lifetime of 0.305 ms.

The luminescence intensity of the electric–dipole $^5D_0 \rightarrow {}^7F_2$ transition is greater than the $^5D_0 \rightarrow {}^7F_1$ magnetic dipole transition, indicating that Eu^{3+} is in an irreversible symmetrical position, which is in line with its single-crystal structure. Single crystals of **EuMOF** were selected and photographed, showing transparency under natural light (Figure S7a) and red luminescence under 365 nm UV irradiation (Figure S7a').

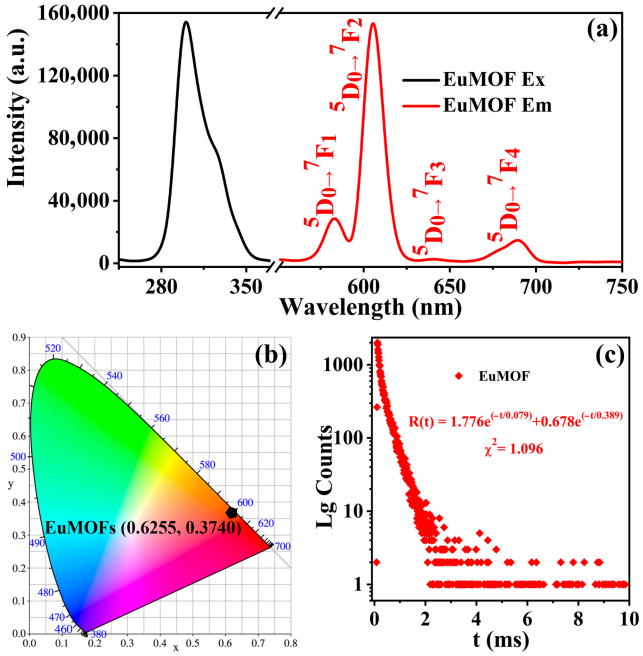

Figure 3. Solid-state photophysical studies for **EuMOF** at room temperature: (**a**) excitation and emission spectra; (**b**) CIE coordinate graph; and (**c**) luminescence decay curve.

3.3. Sensing of Isoprocarb and Lvx

Isoprocarb is often residual in crops and foods, such as fruits and rice, which seriously endangers life and health. Lvx, a fluoroquinolone drug, is a broad-spectrum antibiotic, which is used more and more frequently, causing many diseases. Lvx has a strong ability to resist common biological decomposition, and the excessive use of Lvx is not completely metabolized in the human body and will exist in urine. Therefore, there is an urgent need to explore ultra-sensitive and facile monitoring methods at the molecular level.

In the sensing, 15 kinds of cations of MCl_X or $M(NO_3)_y$, 11 kinds of anions of Na_mX, 24 kinds of organic solvents, seven kinds of amino acids, six kinds of urea, four kinds of tumor markers, four kinds of fluoroquinolone drugs, and four kinds of pesticides, which are listed in the supporting information (Section S1), were prepared in 1.0×10^{-3} M reserve solutions. A total of 50 μL of the above 75 substances solution was mixed with 50 μL of the 1.0×10^{-3} M **EuMOF** reserve solution, 4.9 mL of deionized water, and then the mixed solution was placed at room temperature to react for 1.0 min. The luminescence (excitation at 295 nm, measured in water solution at room temperature at pH about 6.5) histogram monitored at 605 nm ($^5D_0 \rightarrow {}^7F_2$ transition) shows that among the 75 substances, only isoprocarb significantly quenched the luminescence of Eu^{3+} and Lvx significantly enhanced the luminescence of Eu^{3+} (Figure 4a, Figure S8), while other species did not change the luminescence intensity of the solution markedly, suggesting **EuMOF** is a highly selective sensor for isoprocarb and Lvx. In the sensing of isoprocarb, we conducted six repeated detection experiments, where the EuMOF sensor was separated by centrifugation and subsequent extensive water rinsing. It was found that its PXRD was consistent with the as-synthesized sample (Figure S9), and its luminescence intensity did not show significant changes after six rounds of sensing (Figure S10).

In real environments, the sensing results are susceptible to being disturbed by other substances. To investigate whether the detection of isoprocarb and Lvx would be interfered with by other substances, a competition experiment was performed. A total of 4.4 mL deionized water was mixed with 50 μL **EuMOF** stock solution (1.0×10^{-3} M), 50 μL isoprocarb or Lvx solution (1.0×10^{-3} M, H_2O), and 500 μL competitive substance (1.0×10^{-3} M H_2O). The luminescence measurement of **EuMOF** reacting with isoprocarb or Lvx in the

presence of competing substances was determined by the above method. It shows that isoprocarb demonstrates obvious luminescence quenching in the presence of 10 equiv. anti-interference substances (Section S2, Figure 4b, Figure S11). Lvx shows obvious luminescence enhancement in the presence of 10 equiv. anti-interference substances (Section S3, Figure 4c, Figure S12), revealing the high anti-interference of the sensor.

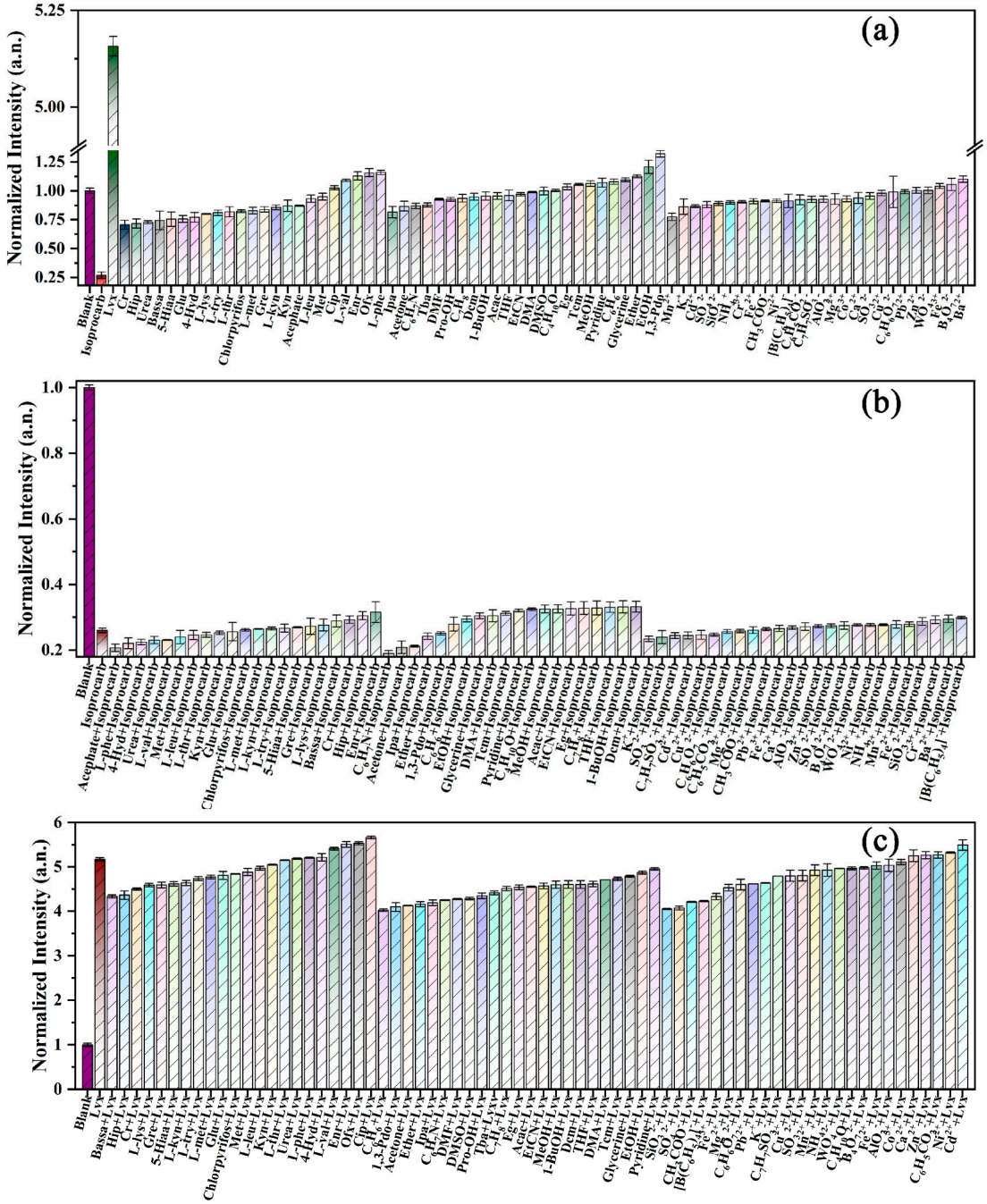

Figure 4. (**a**) A histogram of normalized luminescence intensities at 605 nm of **EuMOF** reacting with 75 substances; (**b**) a histogram of luminescence intensities of **EuMOF** reacting with isoprocarb in the presence of 10 equiv. anti-interference species; and (**c**) a histogram of luminescence intensities of **EuMOF** reacting with Lvx in the presence of 10 equiv. anti-interference species.

In addition, the reaction time of **EuMOF** toward isoprocarb and Lvx was evaluated. The luminescence intensity was monitored at 605 nm ($^5D_0 \rightarrow {}^7F_2$ transition). The dotted line indicates that **EuMOF's** sensing of isoprocarb (Figure 5a) and Lvx (Figure 5b) shows

a fast response time of 15 s, and the sensing signal is stable within 1.0 h, suggesting that **EuMOF** is a highly stable sensor. In order to further understand the sensing characteristics of **EuMOF**, the relationships between the luminescence intensity of the sensor and the concentration of isoprocarb and Lvx were studied. It was found that the luminescence intensity (605 nm) has excellent linear relationships with the concentrations of isoprocarb and Lvx in 0.01–1.6 nM, which have linear equations of $Y = -12565.83023X + 46517.22573$ and $R^2 = 0.99305$ for isoprocarb (Figure 5c), and $Y = 19994.42895X + 44839.92686$ and $R^2 = 0.99162$ for Lvx (Figure 5d). In a wide concentration range of 0.01–10.0 μM, isoprocarb and Lvx concentrations can be determined by luminescence measurement as well, which satisfies the equation of $Y = -3100.24992X + 39164.71282$ and $R^2 = 0.99561$ for isoprocarb (Figure 5e), and $Y = 24130.4125X + 4192.16451$ and $R^2 = 0.99807$ for Lvx (Figure 5f). When 1.0×10^{-9} M isoprocarb reacts with 1.0×10^{-8} M **EuMOF**, the signal-to-noise (S/N) ratio is 5.17 (Figure 5g), revealing its LOD is as low as 1.0 nM through the signal-to-noise method, which is under the LOD value in the Chinese national standard (GB 28260-2011 for isoprocarb is 2.583 μM), indicating that **EuMOF** is a highly sensitive probe for isoprocarb. The LOD for isoprocarb sensing was measured three times, and the relative standard deviation (RSD) of the three-time intra-assay reproducibility is 1.43%.

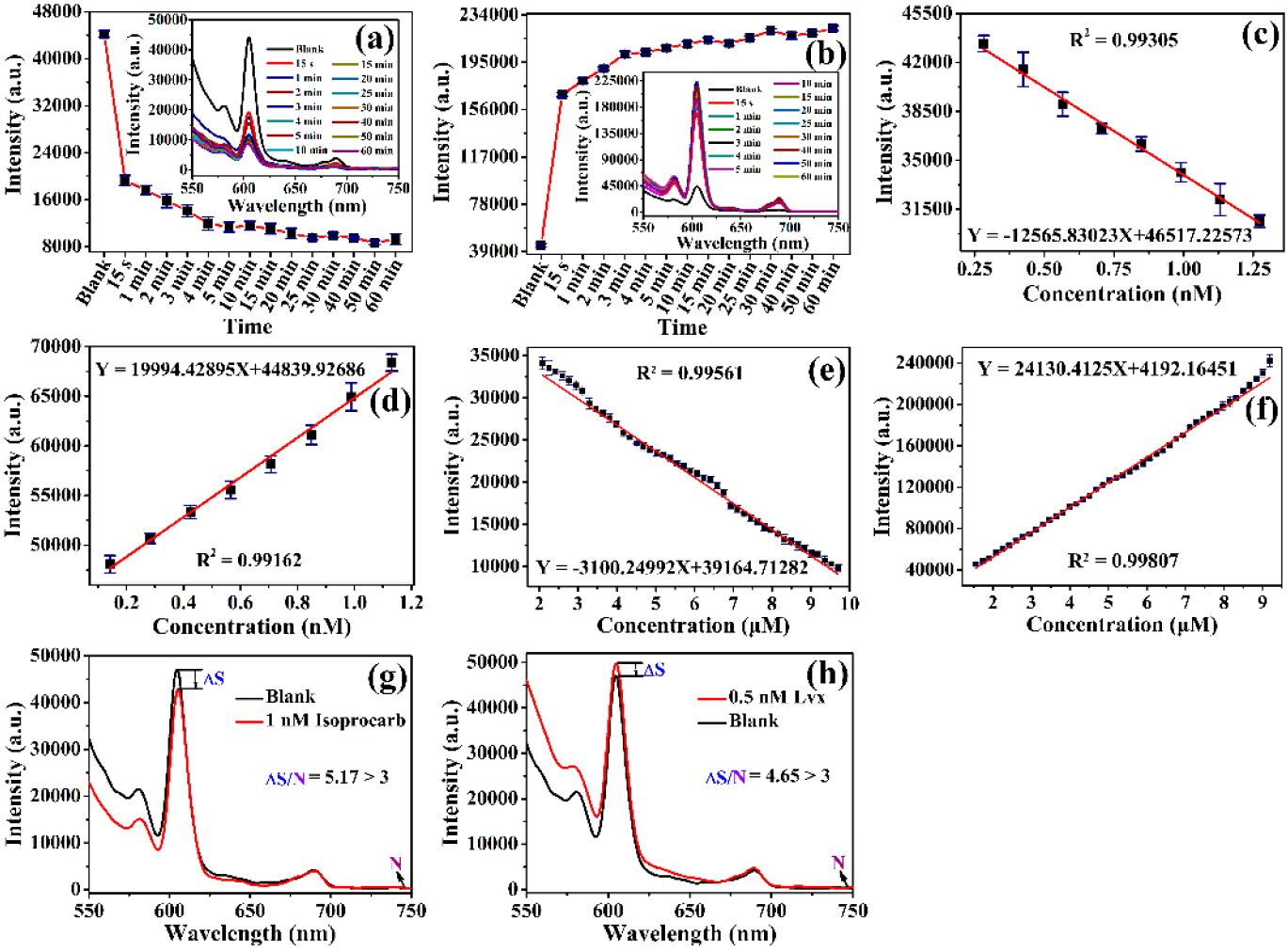

Figure 5. The dot plot of the luminescence intensity at 605 nm of **EuMOF** reacting with isoprocarb (**a**) and Lvx (**b**) at various reaction times. Insert: full emission profiles. The linearity of the luminescence intensity versus the concentration of isoprocarb (**c**) and Lvx (**d**) monitored at 605 nm. The plot of the luminescence intensity (605 nm) of **EuMOF** reacting with 0.01–10.0 μM isoprocarb (**e**) and Lvx (**f**). The LOD measurements for sensing isoprocarb (**g**) and Lvx (**h**).

When 5.0×10^{-10} M Lvx reacted with 1.0×10^{-9} M **EuMOF**, the S/N was 4.65, revealing its LOD is as low as 0.5 nM (Lvx, Figure 5h), using the signal-to-noise ratio method, which is lower than the LOD value of some other sensitive fluorescent probes (Table 1), indicating that **EuMOF** is a highly sensitive probe for Lvx. The LODs for detecting Lvx were measured three times, and the relative standard deviation (RSD) for the three-times intra-assay reproducibility is 2.17%. The recovery rate of the added samples in the sensing of isoprocarb and Lvx is between 97.86 and 101.48% under various conditions, as shown in Table 2.

Table 1. LOD and linear range comparison of different methods for isoprocarb and Lvx detection.

Method	Analyte	Linear Range (nM)	LOD (nM)	References
DPV	Isoprocarb	100–100,000	79	[81]
Amperometry	Isoprocarb	100–150,000	8	[8]
Chronoampermetry	Isoprocarb	5–1000	160	[9]
Luminescent detection	Isoprocarb	300–5200	260	[82]
UV–Vis detector	Isoprocarb	1000–50,000	300	[10]
Differential Pulse Voltammetry	Lvx	5000–1,000,000	1800	[7]
Luminescent detection	Lvx	5000–150,000	850	[2]
Luminescent detection	Lvx	53–110,000	16	[83]
Luminescent detection	Lvx	2500–5000	1260	[6]
Luminescent detection	Lvx	100–400	20	[84]
EuMOF	Isoprocarb	0–9000	1	**This work**
EuMOF	Lvx	0–10,000	0.5	**This work**

Table 2. The recovery results for the determination of isoprocarb and Lvx in water, apple peel supernatant, rice supernatant, and urine using **EuMOF**.

Sample	Analyte	Added (μM)	EuMOF Recovery (%)	Theoretical Value (μM)
Water	Isoprocarb	2.253	98.35	2.424
		3.813	99.85	3.826
		5.372	100.32	5.349
		6.932	98.38	7.024
		8.492	99.45	8.515
Apple peel supernatant	Isoprocarb	2.253	100.12	2.239
		3.813	99.58	3.852
		5.372	99.28	5.428
		6.932	100.37	6.909
		8.492	99.39	8.520
Rice supernatant	Isoprocarb	2.253	100.87	2.174
		3.813	99.12	3.879
		5.372	100.78	5.325
		6.932	99.89	6.937
		8.492	100.57	8.476
Water	Lvx	2.079	99.16	2.060
		3.640	101.48	3.696
		5.199	98.65	5.126
		6.759	100.38	6.785
		8.318	97.86	8.136
		2.079	99.61	2.067
		3.640	101.25	3.698

Table 2. *Cont.*

Sample	Analyte	Added (μM)	EuMOF Recovery (%)	Theoretical Value (μM)
Urine	Lvx	5.199	99.92	5.194
		6.759	100.66	6.810
		8.318	99.57	8.278

In addition, whether **EuMOF** can be used as a luminescent probe for the detection of isoprocarb in actual samples of apple peel (Section S4) and rice supernatant (Section S5), and for the detection of Lvx in urine (Section S6), was further investigated. A total of 4.9 mL apple peel or rice supernatant was mixed with 50 μL **EuMOF** solution (1.0×10^{-3} M, DMF) and 50 μL 1.0×10^{-3} M isoprocarb. A total of 4.9 mL urine solution was mixed with 50 μL stock **EuMOF** solution (1.0×10^{-3} M, DMF) and 50 μL 1.0×10^{-3} M Lvx. This shows that **EuMOF** reacted with isoprocarb in apple peel supernatant, rice supernatant showed obvious luminescence quenching for isoprocarb, and Lvx in urine showed obvious luminescence enhancement, confirming that **EuMOF** has great potential for application in the detection of isoprocarb in real samples of apple peel supernatant, rice supernatant, and Lvx in real urine (Figure 6).

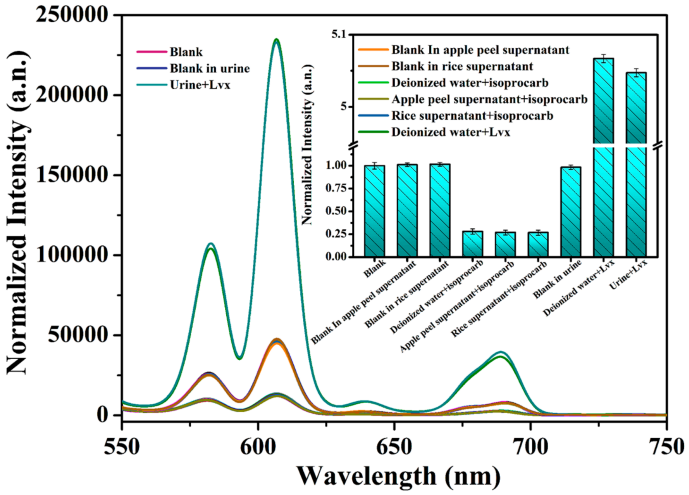

Figure 6. Full spectrum of luminescence of **EuMOF** sensing isoprocarb and Lvx in real samples of apple peel supernatant, rice supernatant, and urine. Insert: luminescence histogram.

It is found that the luminescence intensity (605 nm) has excellent linear relationships with isoprocarb concentration in the range of 0.01–1.6 nM in the real samples of apple peel supernatant and rice supernatant, and has excellent linear relationships with Lvx concentrations in urine, which have linear equations of $Y = -13697.23628X + 46976.39555$ and $R^2 = 0.9925$ for isoprocarb in apple peel supernatant (Figure 7a), $Y = -12652.30395X + 46769.17802$ and $R^2 = 0.9951$ for isoprocarb in rice supernatant (Figure 7b), and $Y = 18104.3278X + 39563.96478$ and $R^2 = 0.99436$ for Lvx in urine (Figure 7c). In a wide concentration range of 0.01–9.0 μM in apple peel and rice preparation solution, isoprocarb concentration can be determined by luminescence measurement as well, which satisfies the equation of $Y = -3436.03363X + 45003.13694$ and $R^2 = 0.99503$ in apple peel supernatant (Figure 7d), and $Y = -4364.02963X + 49589.00671$ and $R^2 = 0.9941$ in rice supernatant (Figure 7e). In the concentration range of 0.01–9.0 μM in urine, Lvx concentration can be determined by luminescence measurement as well, which satisfies the equation of $Y = 23275.10227X + 23158.99165$ and $R^2 = 0.99457$ (Figure 7f). When 1.0×10^{-9} M isoprocarb reacted with 1.0×10^{-8} M **EuMOF** in apple peel and rice supernatant, the

signal-to-noise (S/N) ratios are 4.82 and 5.32, respectively, revealing its LOD is as low as 1.0 nM (Figure 7g,h), which is lower than the LOD value in the Chinese national standard (GB 28260-2011, isoprocarb 2.583 μM), indicating that **EuMOF** is a highly sensitive probe for isoprocarb in apple peel and rice supernatant. When 5.0×10^{-10} M Lvx reacts with 1.0×10^{-9} M **EuMOF** in urine, the signal-to-noise (S/N) ratio is 4.35, suggesting its LOD is as low as 0.5 nM (Figure 7i), which is lower than the LOD value of the other fluorescent probes in Table 2, indicating **EuMOF** is a highly sensitive probe for Lvx in real samples. The recovery rates of isoprocarb and Lvx in the above real samples are between 99.12 and 101.25% (Table 2), further confirming the reliability and practicability of the sensing method in this work.

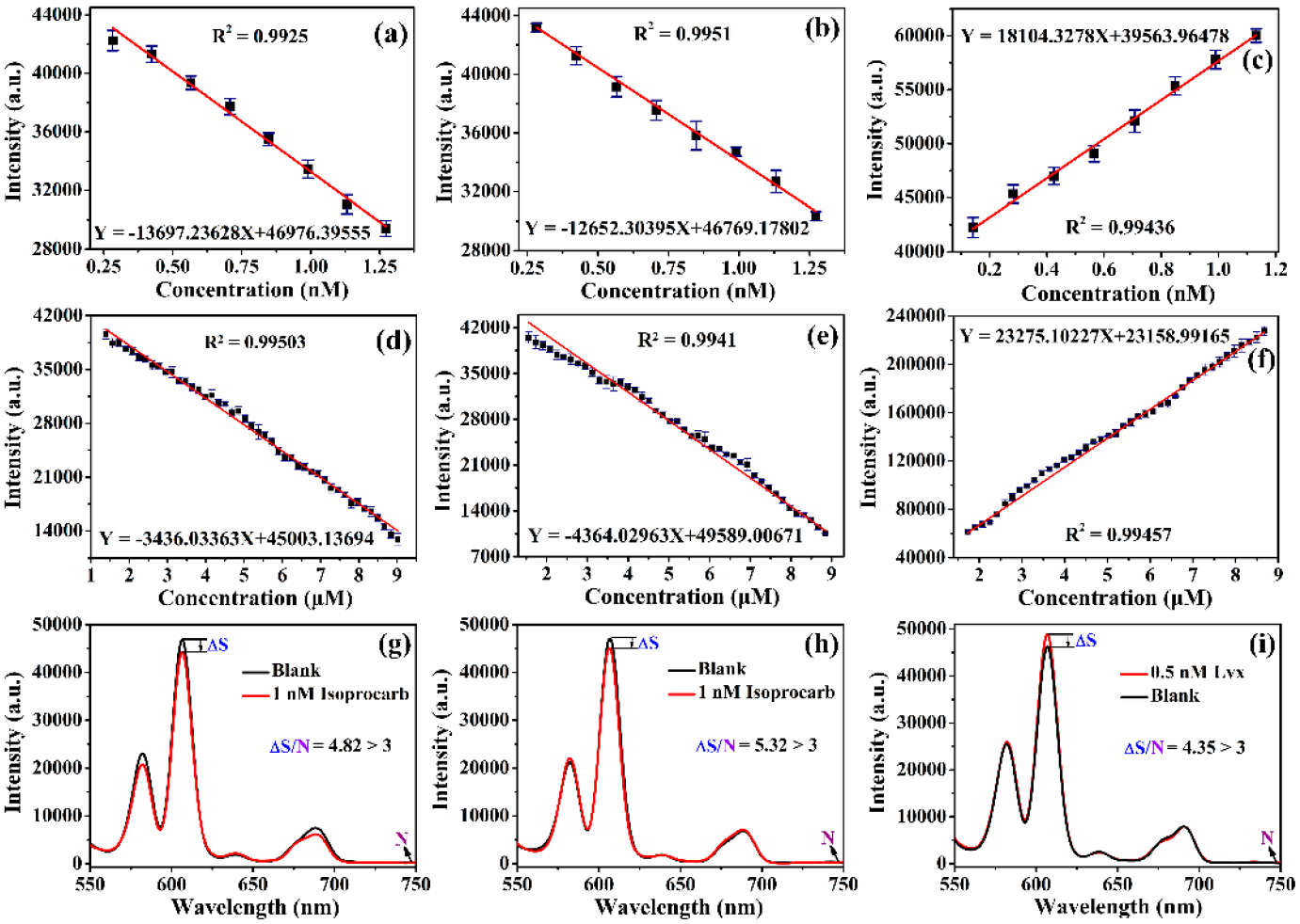

Figure 7. A plot of luminescence intensity (605 nm) of **EuMOF** reacting with isoprocarb in real samples of apple peel supernatant (**a**), rice supernatant (**b**), and with Lvx in real samples of urine (**c**); the linearity of luminescence intensity versus the concentration of 0.01–9.0 μM isoprocarb in apple peel supernatant (**d**), in rice supernatant (**e**), and 0.01–9.0 μM Lvx in urine (**f**) at 605 nm; the LOD measurements for sensing isoprocarb in real samples of apple peel supernatant (**g**), rice supernatant (**h**), and Lvx in real samples of urine (**i**).

The sensing performance is superior to that of the previously reported methods listed in Table 1. Compared with other detection methods, the sensor developed in this work has the advantages of simple preparation, low LOD value, high sensitivity, and a wide linear range.

3.4. Sensing Mechanism

EuMOF that reacted with 1.0×10^{-5} M isoprocarb and Lvx was washed with 3×5.0 mL water and measured by PXRD. The results confirmed that the samples were in line with the as-synthesized **EuMOF**, and no peaks in line with isoprocarb or Lvx appeared, confirming the structure of **EuMOF** remains intact after sensing (Figure S7). The luminescence lifetimes of the **EuMOF** blank solution (1.0×10^{-5} M) and the **EuMOF** solution (1.0×10^{-5} M) reacted with isoprocarb (1.0×10^{-5} M) or Lvx (1.0×10^{-5} M) are 0.281, 0.242, and 1.862 ms (Figure 8a) and the photoluminescence quantum yields are 7.52%, 6.86%, and 13.54%, respectively. This reveals that the lifetimes of the sensing samples for isoprocarb are shorter than those of the blank solution, and those of Lvx are longer than those of the blank solution, and their luminescence quantum yields are in line with their lifetimes, revealing that the sensing of isoprocarb is a dynamic luminescence-quenching process and that of Lvx is a dynamic luminescence-enhancing process.

Among the 75 evaluated sensing species, the sensing of isoprocarb and Lvx may be due to the fact that only the two species can bind to **EuMOF**. The LUMO level of Lvx (−2.2476) is smaller than the LUMO level of isoprocarb (−0.9306) (Figure 8b), and the LUMO level of Lvx is closer to the energy level of Eu^{3+}, which makes it easier to transfer energy to Eu^{3+}, so the luminescence is enhanced. The LUMO energy level of isoprocarb to Eu^{3+} is more suitable for Eu^{3+} than Lvx, so the luminescence of isoprocarb sensing is decreased [85].

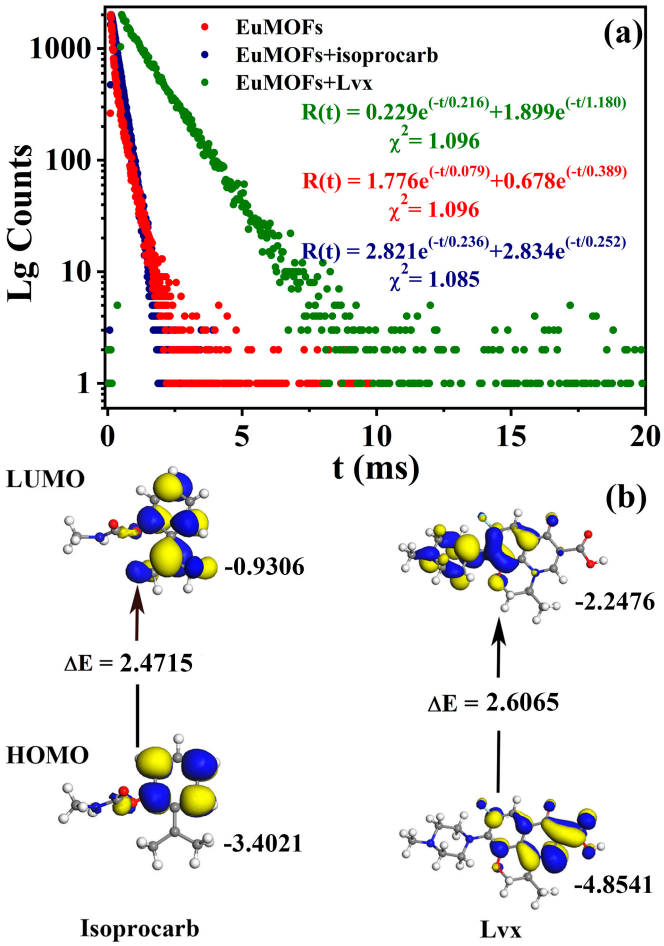

Figure 8. (**a**) Luminescence lifetime decay curves of **EuMOF**, **EuMOF** + isoprocarb, and **EuMOF** + Lvx samples, and (**b**) HOMO and LUMO of isoprocarb and Lvx.

4. Conclusions

In summary, a porous lanthanide MOF (**EuMOF**) was obtained, and its luminescence properties were systematically investigated. Interestingly, **EuMOF** is a bifunctional sensor for isoprocarb and Lvx, showing excellent anti-interference ability, a rapid response of 15 s, an excellent linear relationship and wide linear range, and LODs as low as 1.0 nM and 0.5 nM, respectively. In addition, **EuMOF** was also successfully applied to the detection of isoprocarb in apple peel and rice supernatant and the detection of Lvx in real urine. It maintains high selectivity for isoprocarb and Lvx in actual samples, excellent anti-interference ability, and excellent detection stability in the linear range of 0.01~9.0 nM. The recoveries for the two species sensing were in the range of 99.12%~101.25%. The LOD for isoprocarb detection in apple peel and rice supernatant was as low as 1.0 nM, and for Lvx detection in urine was as low as 0.5 nM, with excellent reproducibility and recovery. The sensor has a higher sensitivity for isoprocarb and Lvx than the maximum residue Chinese national limit levels (GB 28260-2011, isoprocarb 2.583 μM) or previously reported luminescence sensors, respectively. More interestingly, it allows specific detection of isoprocarb residues in crop food samples and Lvx in human urine. Based on the investigation of the luminescence lifetime and DFT, the sensing mechanisms were investigated. As an efficient pesticide response substance, **EuMOF** provides a new detection platform for isoprocarb residues in crops and has great potential application value for food safety and human health. The highly sensitive and quick detection of Lvx in human urine shows extraordinary significance for human health.

Supplementary Materials: The following supporting information can be downloaded at: https://www.mdpi.com/article/10.3390/chemosensors14060144/s1, Figure S1. The synthesis process diagram of **EuMOF**. Figure S2. IR spectra of **EuMOF** and the ligand of 2,2-dihydroxyacetic acid (2,4-DHA). Figure S3. Coordination mode of chelating of the ligand of OA. Figure S4. Single cap twisted quadrilateral coordination environment of Eu^{3+}. Figure S5. The water contact angle of **EuMOF** slices. Figure S6. The SEM image of the as-synthesized **EuMOF**. Figure S7. (a) The photo of crystal morphology of **EuMOF** under day light; (a') The photo of crystal morphology of **EuMOF** under 365 nm UV light. Figure S8. Full spectra of normalized luminescence intensities of **EuMOF** reacting with 75 substances. Figure S9. PXRD of simulated **Eu 2D**, as-synthesized **EuMOF**, **EuMOF** reacted with isoprocarb and Lvx, and isoprocarb and Lvx, respectively. Figure S10. Full luminescence spectra of **EuMOF** reacted to isoprocarb for 6 cycles. Figure S11. Full spectra of normalized luminescence intensities of **EuMOF** reacted to isoprocarb at the presence of 10 equiv. anti-interference species. Figure S12. Full spectra of luminescence intensities of **EuMOF** reacted to Lvx at the presence of 10 equiv. anti-interference species. Table S1. Crystallographic parameters of **EuMOF**. Table S2. Bond lengths [Å] and angles [deg] for **EuMOF** [86–89].

Author Contributions: The work presented here was carried out as a collaboration among all authors. Conceptualization, methodology, and formal analysis, Y.Y., Y.C. and C.Z.; writing—original draft preparation, Y.Y., N.S. and Y.C.; writing—review and editing, N.S. and C.Z.; funding acquisition, C.Z. All authors have read and agreed to the published version of the manuscript.

Funding: This research was funded by the Jiangxi Provincial Natural Science Foundation (20232ACB213006, 20233AAE02007).

Institutional Review Board Statement: This study involving the use of urine samples received ethical clearance from the College of Chemistry and Materials, Jiangxi Normal University. The research was classified as negligible-risk, with no anticipated adverse effects or discomfort to the subjects, and was carried out in compliance with the ethical standards.

Informed Consent Statement: Not applicable.

Data Availability Statement: The data will be made available upon request.

Conflicts of Interest: The authors declare no conflicts of interest.

References

1. Wang, S.; Han, X.; Yu, T.; Liu, Y.; Zhang, H.; Mao, H.; Hu, C.; Xu, X. Isoprocarb causes neurotoxicity of zebrafish embryos through oxidative stress-induced apoptosis. *Ecotoxicol. Environ. Saf.* **2022**, *242*, 113870. [CrossRef] [PubMed]
2. Shi, Y.Q.; Wu, Q.C.; Li, W.T.; Lin, L.; Qu, F.F.; Shen, C.J.; Wei, Y.Z.; Nie, P.C.; He, Y.; Feng, X.P. Ultra-sensitive detection of hydrogen peroxide and levofloxacin using a dual-functional fluorescent probe. *J. Hazard. Mater.* **2022**, *432*, 128605. [CrossRef] [PubMed]
3. Hidalgo, J.; Turdean, G.L.; Vilasó-Cadre, J.E.; Galambos, I.; Reyes-Domínguez, I.A.; Hidalgo, L.; Ignat, N.; Llanos-Lizcano, R. An optimized chemically modified electrode based on copper oxide nanorods for the quantification of chemical oxygen demand in wastewater. *Inorg. Chem. Commun.* **2025**, *179*, 114848. [CrossRef]
4. Hashmi, S.Z.H.; Dhiman, T.K.; Chaudhary, N.; Singh, A.K.; Kumar, R.; Sharma, J.G.; Kumar, A.; Solanki, P.R. Levofloxacin Detection Using l-Cysteine Capped MgS Quantum Dots via the Photoinduced Electron Transfer Process. *Front. Nanotechnol.* **2021**, *3*, 616186. [CrossRef]
5. Surendran, A.P.; Mathew, J.; Varghese, B.; Mathew, B. Myxopyrum serratulum-derived carbon quantum dots for the highly selective and sensitive detection of levofloxacin. *Results Surf. Interfaces* **2025**, *20*, 100621. [CrossRef]
6. Liang, X.; Liu, H.M.; Du, Y.; Li, W.Z.; Wang, M.; Ge, B.; Zhao, L.M. Terbium functionalized covalent organic framework for selective and sensitive detection of LVX based on fluorescence enhancement. *Colloids Surf. A* **2020**, *606*, 125429. [CrossRef]
7. Zhad, H.; Lai, R.Y. Iron(III)-mediated Electrochemical Detection of Levofloxacin in Complex Biological Samples. *Electroanalysis* **2017**, *29*, 2672–2677. [CrossRef]
8. Jiao, W.; Ding, G.Y.; Wang, L.; Liu, Y.; Zhan, T.R. Polyaniline functionalized CoAl-layered double hydroxide nanosheets as a platform for the electrochemical detection of carbaryl and isoprocarb. *Microchim. Acta* **2022**, *189*, 78. [CrossRef]
9. Rachmawati, A.; Sanjaya, A.R.; Putri, Y.; Gunlazuardi, J.; Ivandini, T.A. An acetylcholinesterase-based biosensor for isoprocarb using a gold nanoparticles-polyaniline modified graphite pencil electrode. *Anal. Sci.* **2023**, *39*, 911–923. [CrossRef] [PubMed]
10. Hsu, C.H.; Hu, C.C.; Chiu, T.C. Analysis of carbofuran, carbosulfan, isoprocarb, 3-hydroxycarbofuran, and 3-ketocarbofuran by micellar electrokinetic chromatography. *J. Sep. Sci.* **2012**, *35*, 1359–1364. [CrossRef] [PubMed]
11. Cai, S.T.; Huang, Z.L.; Liu, C.; Liu, Q.C.; Cao, S.H.; Zeng, X.S. A NIR-emitting fluorescent probe based on se-substituted xanthene-cyanine for bioimaging endogenous H_2O_2 in autophagy and tumors. *Spectrochim. Acta A* **2026**, *348*, 127184. [CrossRef]
12. Zhang, N.N.; Wang, H.Y.; Yan, X.Y.; Wang, X.P.; Liu, B.; Zhang, Y.Y.; Yang, Y.G. Deep-red emitting $La_3Ga_5SiO_{14}$:Mn^{4+} phosphors with outstanding thermal stability. *J. Mol. Struct.* **2025**, *1325*, 141066. [CrossRef]
13. Xia, Y.P.; Huang, Y.X.; Li, H.H.; Li, X.T.; Zheng, Z.P.; Zhou, F. Mechanochemical-assisted synthesis of a novel sandwich-structured coronene/trinuclear silver(I) pyrazolate donor-acceptor cocrystal: Structure, spectroscopic, Hirshfeld surfaces and DFT studies. *J. Mol. Struct.* **2025**, *1340*, 142579. [CrossRef]
14. Liu, L.R.; Liu, S.Y.; Han, D.D.; Meng, Q.G.; Niu, C.; Wang, Z.Q.; Xin, X.L. A Multifunctional Cyclodextrin-based Metal-organic Material for the Visual and Selective Detection of Ag^+ and Adsorption of Congo Red. *Curr. Anal. Chem.* **2025**, *22*, 851–860. [CrossRef]
15. Zhou, X.J.; Liu, L.L.; Wu, D.X.; Niu, Y.; Zheng, S.M.; Lu, J.T.; Feng, Y.M.; Tai, X.S. A Luminescent Cd-MOF Used as a Chemosensor for High-Efficiency Sensing of Fe^{3+}, Cr(IV), Trinitrophenol, and Colchicine. *ACS Omega* **2024**, *9*, 11339–11346. [CrossRef] [PubMed]
16. Wang, J.; Song, M.J.; Xue, J.P.; Bi, S.L.; Seo, H.J. Luminescence properties of Bi^{3+}/Sm^{3+} co-doped $K_3Gd_5(PO_4)_6$ phosphors for self-referencing optical thermometry. *RSC Adv.* **2024**, *14*, 31398–31408. [CrossRef] [PubMed]
17. Zeng, W.; Wang, X.; Kong, X.; Li, Y.; Zhang, Y. Study on crystal structure, spectroscopic, thermodynamic properties and Hirshfeld surfaces of a new spirocompound containing thiourea group $C_{17}H_{18}N_2O_4S$. *J. Mol. Struct.* **2023**, *1279*, 135017. [CrossRef]
18. Abdurahman, A.; Wang, J.; Zhao, Y.; Li, P.; Shen, L.; Peng, Q. A Highly Stable Organic Luminescent Diradical. *Angew. Chem. Int. Ed.* **2023**, *62*, e202300772. [CrossRef]
19. Zhou, W.W.; Xv, L.; Zheng, Q.H.; Wang, F.W.; Liu, F.F.; Yue, L.; Qian, Y.W.; Song, M.J.; Xie, Z.; Zhao, W. Sandwich heterometallic coordination polymers consisting of copper-cluster pillars and layered networks of {Ln_6} wheels: Synthesis, structures, spectroscopic properties and Judd-Ofelt analysis. *Transit. Met. Chem.* **2021**, *46*, 555–564. [CrossRef]
20. Yu, M.Y.; Li, X.Z.; Zhang, L.; Jia, Y.L.; Zou, F.; Liu, Z.L.; Zhang, X.W.; Zhang, Q.; Liu, J.H.; Li, W.; et al. Recent Advances in Polyoxometalate-Based Materials as Anodes for Lithium-Ion Batteries. *ChemistrySelect* **2025**, *10*, e03244. [CrossRef]
21. Niu, X.K.; Zheng, N.; Liao, M.L.; Zhu, Q.Q.; Tian, H.Y.; Lu, J.T.; Zhang, X.M. $Cu_{x+1}O$-mediated photo-nanozyme-integrated photoelectrochemical-colorimetric dual-readout biosensing for sensitive detection of MiRNA. *Sens. Actuators B Chem.* **2025**, *444*, 138383. [CrossRef]
22. Liu, J.H.; Liu, D.; Yu, M.Y.; Liu, L.; Wang, Y.Q.; Huo, Y.F.; Sun, S.Q.; Hao, S.S. Manganese-Resorcin 4 Arene-Based Metal-Organic Framework: Syntheses, Structure and Lithium-Ion Battery Application. *Eur. J. Inorg. Chem.* **2025**, *28*, e202400785. [CrossRef]

23. Tai, X.-S.; Wang, L.-H.; Al-Resayes, S.I.; Azam, M. A new 3D Ba(II) coordination polymer based on 3-(3-carboxyphenyl)-isonicotinic acid: Structural studies and its catalytic role in benzylic alcohol oxidation. *Polyhedron* **2026**, *289*, 118009. [CrossRef]
24. Tai, X.S.; Wang, L.H.; Al-Resayes, S.I.; Azam, M. Synthesis, structural characterization, Hirschfeld surface analysis and catalytic application of a new cd(II) complex bearing 1H-pyrazolo 3,4-b pyridine-3-amine and pyridine carboxylic acid. *Polyhedron* **2025**, *279*, 117647.
25. Lu, H.; Fu, D.; Tai, X.S.; Sun, Z.L.; Wang, X.K. Metal-Organic Frameworks/Covalent-Organic Frameworks-Based Materials in Organic/inorganic Pollutant Elimination and CO_2 Reduction Applications. *ChemNanoMat* **2025**, *11*, e202500244. [CrossRef]
26. Liu, L.L.; Zang, M.L.; Li, L.; Zhang, Y.K.; Wang, L.Y.; Zhou, X.J.; Xin, C.L.; Tai, X.S. MIL-53(Al)-derived bimetallic Pd-Co catalysts for the selective hydrogenation of 1,3-butadiene at low temperature. *Sci. Rep.* **2025**, *15*, 448. [CrossRef] [PubMed]
27. Tai, X.S.; Yan, X.H.; Wang, L.H. Synthesis, Structural Characterization, Hirschfeld Surface Analysis, Density Functional Theory, and Photocatalytic CO_2 Reduction Activity of a New Ca(II) Complex with a Bis-Schiff Base Ligand. *Molecules* **2024**, *29*, 1047. [CrossRef] [PubMed]
28. Liu, Y.; Tang, X.; Yan, X.H.; Wang, L.H.; Tai, X.S.; Azam, M.; Zhao, D.Q. The Synthesis, Structural Characterization, and DFT Calculation of a New Binuclear Gd(III) Complex with 4-Aacetylphenoxyacetic Acid and 1,10-Phenanthroline Ligands and Its Roles in Catalytic Activity. *Molecules* **2024**, *29*, 3039. [CrossRef] [PubMed]
29. Cui, Y.; Chen, Y.S.; Cao, Z.; Xu, L.L.; He, J.; Zhu, Z.H.; Lian, L.S.; Luo, X.; Yang, Z.Y.; Chen, M.D. Oxidation of Toluene over the Pt-Embedded Mesoporous CeO_2 Hollow Nanospheres with Advanced Catalytic Performances. *Inorg. Chem.* **2024**, *63*, 19972–19990. [CrossRef] [PubMed]
30. Wang, L.H.; Tai, X.S. Synthesis, Structural Characterization, Hirschfeld Surface Analysis and Photocatalytic CO_2 Reduction Activity of a New Dinuclear Gd(III) Complex with 6-Phenylpyridine-2-Carboxylic Acid and 1,10-Phenanthroline Ligands. *Molecules* **2023**, *28*, 7595. [CrossRef] [PubMed]
31. Wu, Q.; Gao, Q.P.; Sun, L.M.; Guo, H.M.; Tai, X.S.; Li, D.; Liu, L.; Ling, C.Y.; Sun, X.P. Facilitating active species by decorating CeO_2 on Ni_3S_2 nanosheets for efficient water oxidation electrocatalysis. *Chin. J. Catal.* **2021**, *42*, 482–489. [CrossRef]
32. Lu, J.; Zhang, H.; Li, S.; Guo, S.; Shen, L.; Zhou, T.; Zhong, H.; Wu, L.; Meng, Q.; Zhang, Y. Oxygen-Vacancy-Enhanced Peroxidase-like Activity of Reduced Co_3O_4 Nanocomposites for the Colorimetric Detection of H_2O_2 and Glucose. *Inorg. Chem.* **2020**, *59*, 3152–3159. [CrossRef] [PubMed]
33. Lu, J.T.; Zeng, Y.; Ma, X.X.; Wang, H.Q.; Gao, L.N.; Zhong, H.; Meng, Q.G. Cobalt Nanoparticles Embedded into N-Doped Carbon from Metal Organic Frameworks as Highly Active Electrocatalyst for Oxygen Evolution Reaction. *Polymers* **2019**, *11*, 828. [CrossRef] [PubMed]
34. Zhang, S.; Lu, L.; Jiang, J.; Liu, N.; Zhao, B.; Xu, M.; Cheng, P.; Shi, W. Organizing Photosensitive and Photothermal Single-Sites Uniformly in a Trimetallic Metal-Organic Framework for Efficient Photocatalytic Hydrogen Evolution. *Adv. Mater.* **2024**, *36*, 2403464. [CrossRef]
35. Zhao, X.Y.; Chang, X.T.; Qin, C.X.; Wang, X.K.; Xu, M.M.; Fan, W.D.; Meng, Q.G.; Sun, D.F. Solvent Regulation in Layered Zn-MOFs for C_2H_2/CO_2 and CO_2/CH_4 Separation. *Molecules* **2025**, *30*, 1171. [CrossRef] [PubMed]
36. Xu, M.M.; Li, Y.; Wang, X.K.; Liu, H.Y.; Liu, Q.R.; Zhang, Y.F.; Fan, W.D.; Meng, Q.G.; Sun, D.F. Imidazole-Functionalized Zn-MOFs for One-Step C_2H_4 Purification from $C_2H_2/C_2H_4/C_2H_6$ Ternary Mixture. *Inorg. Chem.* **2025**, *64*, 813–817. [CrossRef] [PubMed]
37. Gao, X.; Yan, W.H.; Hu, B.Y.; Huang, Y.X.; Zheng, S.M. Porous Metal-Organic Frameworks for Light Hydrocarbon Separation. *Molecules* **2023**, *28*, 6337. [CrossRef] [PubMed]
38. Xin, C.L.; Ren, Y.; Zhang, Z.F.; Liu, L.L.; Wang, X.; Yang, J.M. Enhancement of Hydrothermal Stability and CO_2 Adsorption of Mg-MOF-74/MCF Composites. *ACS Omega* **2021**, *6*, 7739–7745. [CrossRef] [PubMed]
39. Wang, L.H.; Tai, X.S.; Azam, M.; Sui, B.L.; Wang, A.L. Synthesis, structural characterization, and Hirschfeld surface analysis of a novel Mn(II) complex based on N-acetyl-L-phenylalanine ligand and its evaluation as a cytotoxic agent. *Polyhedron* **2025**, *279*, 117659. [CrossRef]
40. Chen, W.; Sun, J.R.; Xiao, H.Y.; Zhu, Z.F.; Xing, J.Q.; Zhang, Y.B.; Shen, L.; Wang, Y.F. Near-infrared hemicyanine photosensitizer for targeted mitochondrial viscosity imaging and efficient photodynamic therapy. *Spectrochim. Acta A* **2025**, *325*, 125049. [CrossRef]
41. Cao, S.H.; Tai, X.S.; Li, K.X.; Zhang, A.L.; Ma, P.J.; Sui, G.Q.; Zhang, L.S.; Tian, X.H.; Wang, A.L.; Azam, M. Two novel homo/hetero polynuclear complexes for DNA binding, molecular docking and anti-cancer activity. *J. Mol. Struct.* **2025**, *1325*, 141040. [CrossRef]
42. Cao, S.H.; Liu, Y.C.; Tai, X.S.; Shen, L.; Yang, H.K.; Li, F.H.; Sui, B.L.; Ma, P.J.; Zhu, L.X.; Gao, B.; et al. A dual-type I/II NIR photosensitizer for effective cancer photodynamic therapy with enhanced ROS generation. *RSC Adv.* **2025**, *15*, 28889–28896. [CrossRef] [PubMed]

43. Yang, Y.D.; Niu, X.K.; Duan, B.Q.; Lu, J.T.; Zhang, X.M. Dual-modal biosensor for mercuric ion detection based on $Cu_2O@Cu_2S$/D-TA COF heterojunction with excellent catalase-like, electrochemical and photoelectrochemical properties. *Biosens. Bioelectron.* **2024**, *262*, 116568. [CrossRef] [PubMed]
44. Cao, S.H.; Wang, A.L.; Li, K.X.; Lin, Z.T.; Yang, H.W.; Zhang, X.L.; Qiu, J.M.; Tai, X.S. A novel tetranuclear Cu(ii) complex for DNA-binding and in vitro anticancer activity. *RSC Adv.* **2023**, *13*, 26324–26329. [CrossRef] [PubMed]
45. Cao, S.H.; Tai, X.S.; Xin, C.L. Synthesis, Crystal Structure and Antitumor Activity of a Ca(II) Coordination Polymer Based on 4-Acetylphenoxyacetate Ligands. *Chin. J. Struct. Chem.* **2021**, *40*, 324–328.
46. Tai, X.S.; Zhou, X.J.; Liu, L.L. Synthesis, Crystal Structure and Antitumor Activity of a Na(I) Coordination Polymer Based on 2-Propyl-4,5-imidazoledicarboxylic Acid and 1,10-Phenanthroline Ligands. *Chin. J. Struct. Chem.* **2019**, *38*, 1079–1085.
47. Xie, N.B.; Wang, M.; Ji, T.T.; Guo, X.; Gang, F.Y.; Hao, Y.; Zeng, L.; Wang, Y.F.; Feng, Y.Q.; Yuan, B.F. Simultaneous detection of 5-methylcytosine and 5-hydroxymethylcytosine at specific genomic loci by engineered deaminase-assisted sequencing. *Chem. Sci.* **2024**, *15*, 10073–10083. [CrossRef] [PubMed]
48. Cai, D.G.; Pan, S.F.; Zheng, T.F.; Cao, C.; Hu, Z.B.; Peng, Y.; Wu, Y.Q.; Wen, H.R.; Liu, S.J. pH- and Solvent-Stable Zn^{II}/Cd^{II} Metal-Organic Frameworks with 2,1,3-Benzothiadiazole Derivative for Turn-On Fluorescence Sensing Dipicolinic Acid and Thiamine in Living Cells. *Anal. Chem.* **2026**, *98*, 5205–5213. [CrossRef] [PubMed]
49. Li, H.H.; Wu, Y.; Shoaib, M.; Sheng, W.; Bei, Q.Y.; Murugesan, A. Lanthanide-Doped Upconversion Luminescence: A New Frontier in Pathogenic Bacteria and Metabolite Detection from Design to Point-of-Care Application. *Chemosensors* **2025**, *13*, 60. [CrossRef]
50. Xia, Z.R.; Li, R.Q.; Liu, F.F.; Zhou, W.W.; Zhao, W.; Meng, W.; Song, M.J.; Xue, J.P. Dual-luminescent $Sc_2(MoO_4)_3$:Dy^{3+}/Eu^{3+} phosphor system: Energy transfer dynamics and high-sensitivity temperature sensing. *RSC Adv.* **2025**, *15*, 28994–29002. [CrossRef] [PubMed]
51. Song, M.J.; Zhou, W.W.; Wang, J.; Wang, M.Q.; Zhao, J.Q.; Ran, W.G. Multicolor luminescence and high efficient optical thermometric performance of Eu^{3+} and Sm^{3+} in self-activated $Na_2LuMg_2V_3O_{12}$ garnet. *J. Rare Earths* **2025**, *43*, 2357–2367. [CrossRef]
52. Song, M.; Wang, J.; Xie, Z.; Liu, L.; Zhao, W.; Zhou, W. Spectroscopic and temperature sensing properties of Sm^{3+} in self-activated $CsLu(WO_4)_2$ phosphors. *J. Rare Earths* **2024**, *42*, 2033–2042. [CrossRef]
53. Cao, E.S.; Zhang, Y.X.; Sun, L.; Sun, B.; Hao, W.T.; Zhang, Y.J.; Nie, Z.Q. WO_3-$LaFeO_3$ Nanocomposites for Highly Sensitive Detection of Acetone Vapor at Low Operating Temperatures. *Chemosensors* **2023**, *11*, 439. [CrossRef]
54. Wang, H.-L.; Li, Y.-L.; Zou, H.-H.; Liang, F.-P.; Zhu, Z.-H. Smart Lanthanide Metal-Organic Frameworks with Multicolor Luminescence Switching Induced by the Dynamic Adaptive Antenna Effect of Molecular Rotors. *Adv. Mater.* **2025**, *37*, 2502742. [CrossRef]
55. Li, Y.-L.; Wang, H.-L.; Zhu, Z.-H.; Liang, F.-P.; Zou, H.-H. Recent advances in the structural design and regulation of lanthanide clusters: Formation and self-assembly mechanisms. *Coord. Chem. Rev.* **2023**, *493*, 215322. [CrossRef]
56. Zhao, D.; Guo, L.; Li, Q.; Yue, C.; Han, B.; Liu, K.; Li, H. Multi-Functional Lanthanide Metallopolymer: Self-Healing and Photo-Stimuli-Responsive Dual-Emitting Luminescence for Diverse Applications. *Adv. Mater.* **2024**, *36*, 2405164. [CrossRef]
57. Ahmed, D.; Spagnoli, E.; Chakir, A.; Mancinelli, M.; Ferroni, M.; Mehdaoui, B.; El Bouari, A.; Fabbri, B. $PrFeTiO_5$-Based Chemoresistive Gas Sensors for VOCs Detection. *Chemosensors* **2025**, *13*, 222. [CrossRef]
58. Lopes, G.P.; Rossato, J.H.H.; Carreno, N.L.V.; Nantes, I.L.; Escote, M.T. Eu-Doped Nickelate as a Platform for an Enzyme-Based Resistive Biosensor for Glucose. *Chemosensors* **2025**, *13*, 387. [CrossRef]
59. Yu, Q.B.; Wang, M.; Feng, X.J.; Li, X.H. Research Progress of Rare Earth Metal-Organic Frameworks on Pollutant Monitoring. *Chemosensors* **2025**, *13*, 184. [CrossRef]
60. Zhou, X.; Guo, X.; Liu, L.; Zhai, H.; Meng, Q.; Shi, Z.; Tai, X. Two d^{10} luminescent metal–organic frameworks as dual functional luminescent sensors for (Fe^{3+},Cu^{2+}) and 2,4,6-trinitrophenol (TNP) with high selectivity and sensitivity. *RSC Adv.* **2020**, *10*, 4817–4824. [CrossRef] [PubMed]
61. Wang, Q.; Dong, J.; Li, Z.; Wang, X.; He, Y.; Chen, B.; Zhao, D. Dual-Emitting Mixed-Lanthanide Metal-Organic Framework for Ratiometric and Quantitative Visual Detection of 2,6-Pyridine Dicarboxylic Acid. *Inorg. Chem.* **2023**, *62*, 14439–14447. [CrossRef] [PubMed]
62. Pan, J.; Lu, J.; Shang, Y.; Li, Y.; Yan, B. Tb(iii)-functionalized MOF hybridized bis-crosslinked networked hydrogel luminescent films for arginine and dopamine hydrochloride sensing and anticounterfeiting. *J. Mater. Chem. C* **2025**, *13*, 1198–1206. [CrossRef]
63. Yu, H.; Yang, X.; Lv, X.; Huang, X. Construction of a 12-metal Zn(II)-Nd(III) nanocluster for ratiometric fluorescence detection of inflammatory marker neopterin. *J. Rare Earths* **2025**, *43*, 270–275. [CrossRef]
64. Sun, Y.; Wang, X.; Liu, S.; Yang, X.; Ren, X.; Liu, W.; Liu, W. Functional Construction of a Novel Lanthanide MOF for Efficient Ratio Luminescence Detection of Ethanol Vapor. *Adv. Opt. Mater.* **2024**, *12*, 2400692. [CrossRef]
65. Wang, M.; Han, Z.; Wang, K.; Zhao, B.; Sun, T.; Wu, Y.; Cheng, P.; Shi, W. Confinement of P-Xylene in the Pores of a Bilanthanide Metal-Organic Framework for Highly Selective Recognition. *Angew. Chem. Int. Ed.* **2024**, *63*, e202318722. [CrossRef]

66. Jiang, Y.; Du, Z.; Qiu, H.; Lin, X.; Yang, Y.; Zeng, C. Regulation of the Metal Center in Lanthanide Nanoparticles to Achieve Multifunctional Sensing. *Anal. Chem.* **2024**, *96*, 12692–12700. [CrossRef] [PubMed]
67. Chen, J.; Liu, P.; Wang, W.; Peng, H.; Ding, L.; Zhou, Y.; Yao, J.; Zeng, C. Luminescence Turn-on of Lanthanide Coordination Polymers Triggered by Norfloxacin for Visual Detection and Anti-Counterfeiting. *Anal. Chem.* **2025**, *97*, 19283–19293. [CrossRef] [PubMed]
68. Dong, Y.L.; Song, W.; Hu, J.; Ren, C.L. A Facile Solid-Phase Synthesis of Scandium-Modified Carbon Dots for Fluorescent Sensing of Cu^{2+}. *Chemosensors* **2025**, *13*, 430. [CrossRef]
69. Kotnana, G.; Hong, S.G. Recent Progress on Rare Earth Orthoferrites for Gas-Sensing Applications. *Chemosensors* **2025**, *13*, 156. [CrossRef]
70. Xia, Y.P.; Zhu, X.S.; Yang, H.; Zhou, F.; Zhu, R.X.; Zhang, Y.T.; Zheng, S.R.; Zheng, Z.P. Synthesis, crystal structure, spectroscopic and theoretical studies of a new fluorescent heterocyclic compound containing diketopyrrolopyrrole (DPP) moiety. *J. Mol. Struct.* **2024**, *1318*, 139334. [CrossRef]
71. Zeng, W.L.; Wang, X.; Zhang, Y.J. Synthesis, Crystal Structures, and Density Functional Theory Studies of Two Salt Cocrystals Containing Meldrum's Acid Group. *ACS Omega* **2022**, *7*, 25132–25139. [CrossRef] [PubMed]
72. Stephens, P.J.; Devlin, F.J.; Chabalowski, C.F.; Frisch, M.J. Ab Initio Calculation of Vibrational Absorption and Circular Dichroism Spectra Using Density Functional Force Fields. *J. Phys. Chem.* **1994**, *98*, 11623–11627. [CrossRef]
73. Xi-Shi, T.; Li-Hua, W.; Al-Resayes, S.I.; Azam, M. A novel Ca(II) coordination polymer with 3-(3-carboxyphenyl)-isonicotinic acid: Design, DFT analysis, and catalytic efficiency. *BMC Chem.* **2026**, *20*, 55. [CrossRef] [PubMed]
74. Sui, B.-L.; Wang, L.-H.; Tai, X.-S.; Al-Resayes, S.I.; Azam, M.; Wang, A.-L. Synthesis, structural characterization, DFT calculation, and antitumor activity of a new Co(II) complex based on 2-((2′-Carboxybenzyl)oxy)benzoic acid and 2,2′-bipyridine ligands. *BMC Chem.* **2026**, *20*, 51. [CrossRef] [PubMed]
75. Zeng, W.L.; Yue, D.Y.; Wang, X.; Kong, X.J. Vibrational spectroscopy, DFT calculations, MEP, NBO, NLO and Hirshfeld surface studies of a new Meldrum's acid derivative containing 2-hydroxyphenylamino moiety. *J. Mol. Struct.* **2025**, *1341*, 142675. [CrossRef]
76. Ding, R.; Liu, J.J.; Meng, Q.G.; Wang, T.; Zhang, X.M. Dual-functional flexible cationic porphyrin-based covalent organic frameworks for selective adsorption and sensitive detection of Cr(VI). *Sep. Purif. Technol.* **2025**, *359*, 130544. [CrossRef]
77. Tai, X.-S.; Wang, L.-H.; Al-Resayes, S.I.; Azam, M. Design, Structural Characterization, and Fluorescence Behavior of a New Centrosymmetric Dinuclear Cd(II) Complex with 2-Formylphenoxyacetic Acid and 1,10-Phenanthroline. *J. Spectrosc.* **2026**, *2026*, 9957210. [CrossRef]
78. Wang, L.H.; Yan, X.H.; Tai, X.S.; Al-Resayes, S.I.; Azam, M. Design and Structural Investigation, Hirschfeld Surface Analysis, and Photoluminescent Behavior of a Cd(II) Coordination Polymer with 4-Acetylphenoxyacetic Acid Ligand. *J. Spectrosc.* **2026**, *2026*, 3903190.
79. Xia, Y.P.; Huang, Y.X.; Zhou, F.; Huang, Z.R.; Yan, J.W.; Lv, J.H.; Tang, F.F. Synthesis, crystal structure, spectroscopic, DFT calculation and GCMC simulation studies of a new Cu(II) metal-organic framework based on 5-(1H-1,2,4-triazol-1-yl)isophthalic acid. *Polyhedron* **2025**, *281*, 117748. [CrossRef]
80. Wang, K.; Zhu, Y.L.; Zheng, T.F.; Xie, X.; Chen, J.L.; Wu, Y.Q.; Liu, S.J.; Wen, H.R. Highly pH-Responsive Sensor Based on a Eu^{III} Metal-Organic Framework with Efficient Recognition of Arginine and Lysine in Living Cells. *Anal. Chem.* **2023**, *95*, 4992–4999. [CrossRef] [PubMed]
81. Della Pelle, F.; Angelini, C.; Sergi, M.; Del Carlo, M.; Pepe, A.; Compagnone, D. Nano carbon black-based screen printed sensor for carbofuran, isoprocarb, carbaryl and fenobucarb detection: Application to grain samples. *Talanta* **2018**, *186*, 389–396. [CrossRef] [PubMed]
82. Zhu, Y.A.; Wang, M.; Zhang, X.G.; Cao, J.; She, Y.X.; Cao, Z.; Wang, J.; Abd El-Aty, A.M. Acetylcholinesterase Immobilized on Magnetic Mesoporous Silica Nanoparticles Coupled with Fluorescence Analysis for Rapid Detection of Carbamate Pesticides. *ACS Appl. Nano Mater.* **2022**, *5*, 1327–1338. [CrossRef]
83. Gao, R.R.; Qiu, Q.; Dong, W. Visual Monitoring of Levofloxacin in Biofluids by Europium(III)-Functionalized Mesoporous Silica Nanoparticles. *ACS Appl. Nano Mater.* **2022**, *5*, 5631–5639. [CrossRef]
84. Su, Y.Q.; Fu, L.S.; Cui, G.H. Two chemically robust Cd(ii)-frameworks for efficient sensing of levofloxacin, benzaldehyde, and Fe^{3+} ions. *Dalton Trans.* **2021**, *50*, 15743–15753. [CrossRef] [PubMed]
85. Zeng, W.L.; Yue, D.Y.; Wang, X.; Li, H.Y.; Kong, X.J. Synthesis, structural, spectroscopic investigation, Hirshfeld surface analysis and DFT calculation of a new spiro compound including 4-nitroaniline moiety. *J. Mol. Struct.* **2025**, *1322*, 140371. [CrossRef]
86. Sheldrick, G.M. Crystal structure refinement with SHELXL. *Acta Crystallogr. Sect. C-Struct. Chem.* **2015**, *71*, 3–8. [CrossRef]
87. Liu, M.; Li, Z.; Xiong, J.; Jiang, Y.; Tang, T.; Qiu, J.; Yao, J.; Ng, S.W.; Zeng, C. Structure regulation for ultra-high luminescence quantum yield lanthanide complex and simultaneous detection of cancer marker and ferrous ion. *J. Rare Earth* **2021**, *39*, 1194–1203. [CrossRef]

88. Barbhuiya, R.I.; Singha, P.; Asaithambi, N.; Singh, S.K. Ultrasound-assisted rapid biological synthesis and characterization of silver nanoparticles using pomelo peel waste. *Food Chem.* **2022**, *385*, 132602. [CrossRef] [PubMed]
89. Wang, Q.; Yin, H.S.; Zhou, Y.L.; Wang, J.; Ai, S.Y. Investigation of the inhibited biotoxicity of heavy metals towards 5-formylcytosine in rice by hydrochar based on photoelectrochemical biosensor. *J. Hazard. Mater.* **2021**, *414*, 125293. [CrossRef] [PubMed]